Supplementary information for

"All-in-One" Hall Rectenna Surpassing 100 GHz Bandwidth

Zhen Hu[1,7], Xiaokai Pan[1,7], Raihan Ahammed[2], Ziteng Zhang[1,7], Fang Wang[1,7], Bo Yin[4], Libo Zhang[3], Yingdong Wei[1,9], Fucong Fei[5], Zhijun Wang[4], Lei Ye[8], Xinglong Wu[6], Fengqi Song[5], Yang Xu[4], Wei Lu[1,7,9], Amit Agarwal[2], Lin Wang[1,7,9]*, Weida Hu[1,3,7]*, and Xiaoshuang Chen[1,3,7,9]

[1]State Key Laboratory of Infrared Physics, Shanghai Institute of Technical Physics, Chinese Academy of Sciences, Shanghai, China.

[2]Department of Physics, Indian Institute of Technology Kanpur, Kanpur, India.

[3]College of Physics and Optoelectronic Engineering, Hangzhou Institute for Advanced Study, University of Chinese Academy of Sciences, Hangzhou, China.

[4]Beijing National Laboratory for Condensed Matter Physics, Institute of Physics, Chinese Academy of Sciences, Beijing, China.

[5]National Laboratory of Solid-state Microstructures, Collaborative Innovation Center of Advanced Microstructures, and School of Physics, Nanjing University, Nanjing, China.

[6]Key Laboratory of Modern Acoustics, MOE, Institute of Acoustics and Collaborative Innovation Center of Advanced Microstructures, National Laboratory of Solid State Microstructures, Nanjing University, Nanjing, China.

[7]University of Chinese Academy of Sciences, Beijing, China.

[8]School of Optical and Electronic Information and Wuhan National Laboratory for Optoelectronics, Huazhong University of Science and Technology, Wuhan, 430074, China

[9]School of Physical Science and Technology, ShanghaiTech University, Shanghai, China.

This file includes:

I. Additional data for density functional theory calculations in $NbIrTe_4$

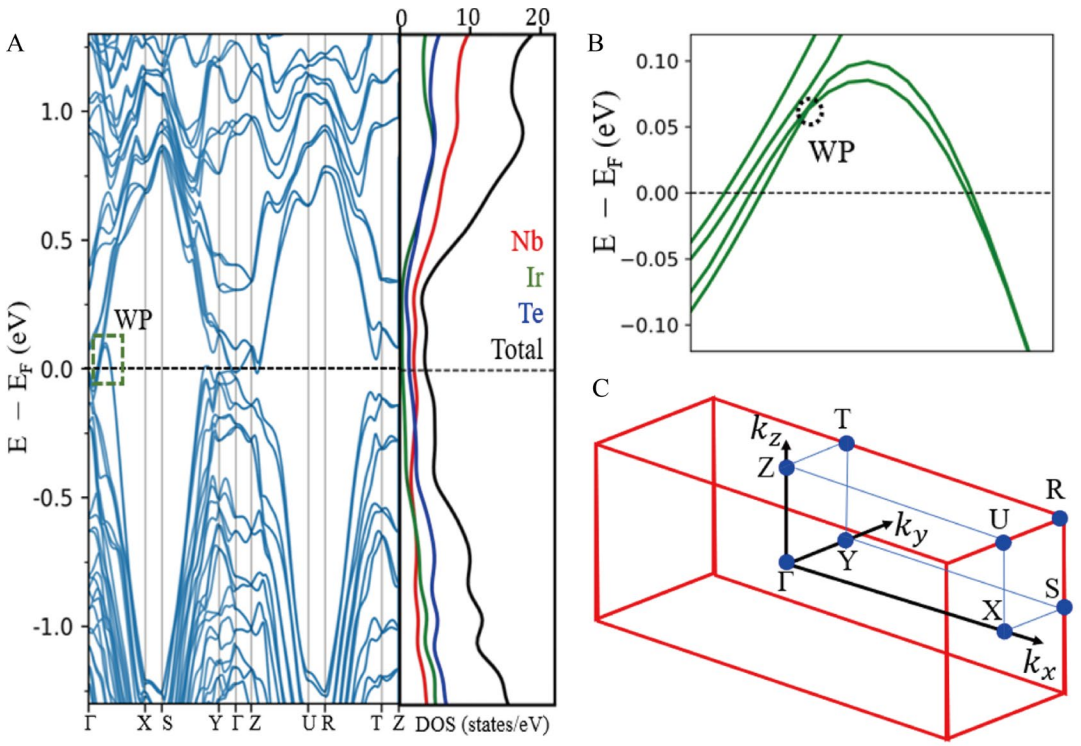

Fig. S1. A. Bulk band structure and density of states (DOS) of $NbIrTe_4$. **B.** Zoomed view of band structure around the Weyl point (WP). **C.** First Brillouin zone (BZ) indicating the high-symmetric k-points.

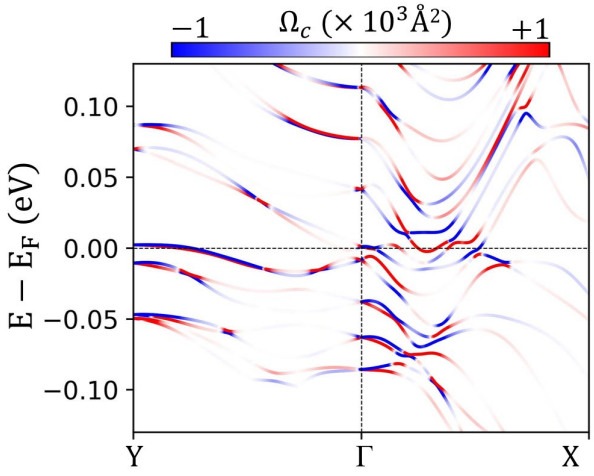

Fig. S2. Berry curvature (BC) projected electronic band structure of six-layer slab Hamiltonian, constructed from bulk Wannier TB Hamiltonian of bulk $NbIrTe_4$.

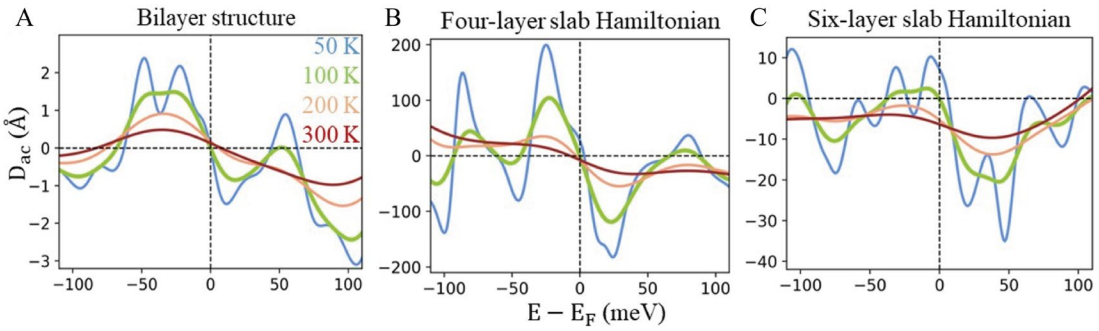

Fig. S3. Temperature dependent berry curvature dipole, BCD (D_{ac}) of (**A**) bilayer structure, (**B**) four-layer slab Hamiltonian, and (**C**) six-layer slab Hamiltonian.

II. Basic characterization of non-centrosymmetric material

II.1. Thickness and element determination

After the transferred devices were etched using focused ion beam technology, standard hall bar devices, cross-geometry devices, and multi-terminal devices were prepared. The SEM images in Fig. S4A how the resulting structures, including the damage diagram caused by the ion beam current on the material edge. However, this damage is considered negligible and does not affect subsequent device preparation (inset of Fig. S4E).

EDS spectrum analysis was also employed to test the element content of the sample and ensure that the material's element composition and content were consistent (Figure S4). In addition, the thickness of the device was measured using an atomic force microscope, as depicted in Figure S4.

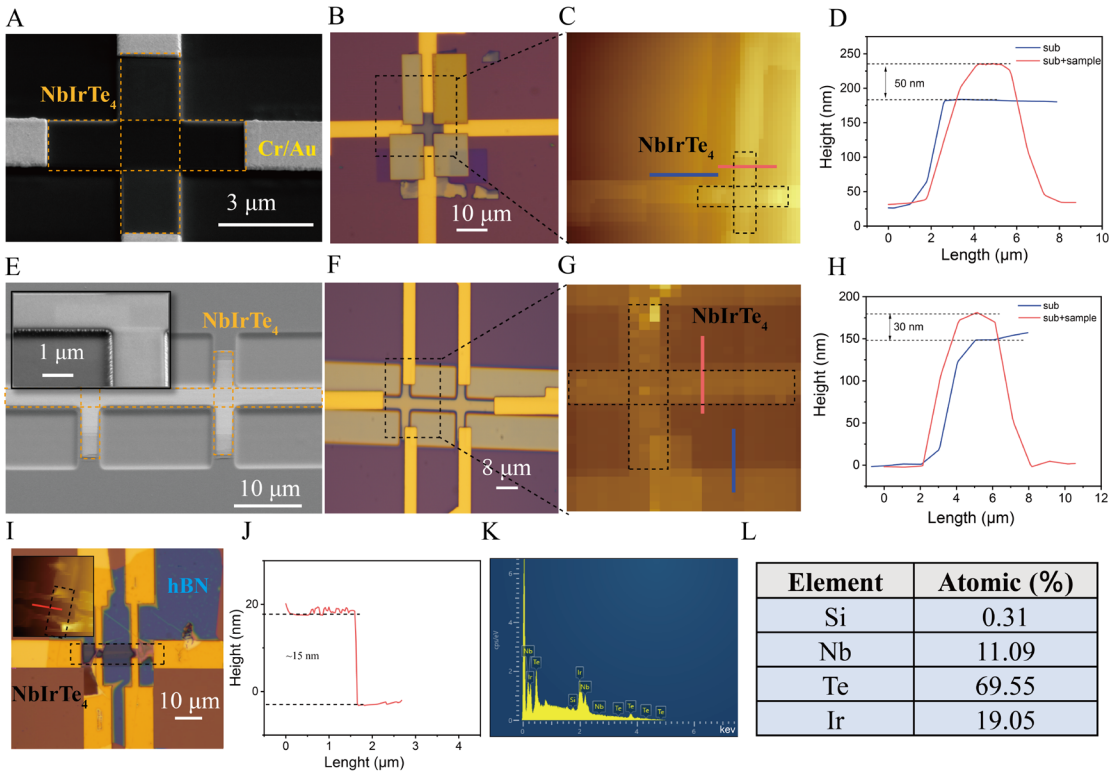

Element	Atomic (%)
Si	0.31
Nb	11.09
Te	69.55
Ir	19.05

Fig. S4. Crytal characterization for the main devices of our measurements. A-C. SEM, microscope and AFM image of crossed-geometry device, respectively. **D.** AFM thickness data along the red and blue line in panel **C**. **E-H.** Same as panels **A-D** but for standard Hall bar device. In inset of **E**, magnified SEM image of $NbIrTe_4$ edge after FIB etching. **I-J.** Same as panels **A-D** but for standard Hall bar device not etched by FIB. **K.** EDS spectrum for the bulk structures. **L.** the elements proportion of the surface and bulk structure.

II.2. The symmetry constraint of non-centrosymmetric material in T_d-$NbIrTe_4$

For T_d-$NbIrTe_4$ (Pmn21), inversion symmetry is broken, but mirror symmetry M_a and glide mirror symmetry $\bar{M}_b$ are preserved. The M_a plane is perpendicular to the $\boldsymbol{a}$-axis, and $\bar{M}_b$ reflections along the $\boldsymbol{b}$-axis involve a half-unit-cell translation along the c-axis (see Figs. S5A-B). In the bulk T_d phase, allowed BCD responses are D_{ab} and D_{ba}, related to nonlinear Hall currents $J_c \propto D_{ab}E_a^2$ or $J_c \propto D_{ba}E_b^2$. Measuring J_c requires access to both the top and bottom sides of the device, which is unfavorable for standard planar geometries. In addition, in the bulk phase, D_{ac} and D_{bc} are zero, so no in-plane nonlinear Hall current is generated (middle panels of Figs. S5D).

For a finite-thickness $NbIrTe_4$ (space group Pm11), broken translational symmetry

along the ***c***-axis removes the glide axis $\bar{M}_b$, but retains mirror plane M_a (Figs. S5B). This reduced symmetry allows only the top and bottom surfaces to exhibit BCD responses: $D_{ac} > 0$. Thus, without an external magnetic field, an a.c. electric field along the ***a***-axis induces a nonlinear Hall voltage along the ***b***-axis, prerequisite for generating the NLHE.

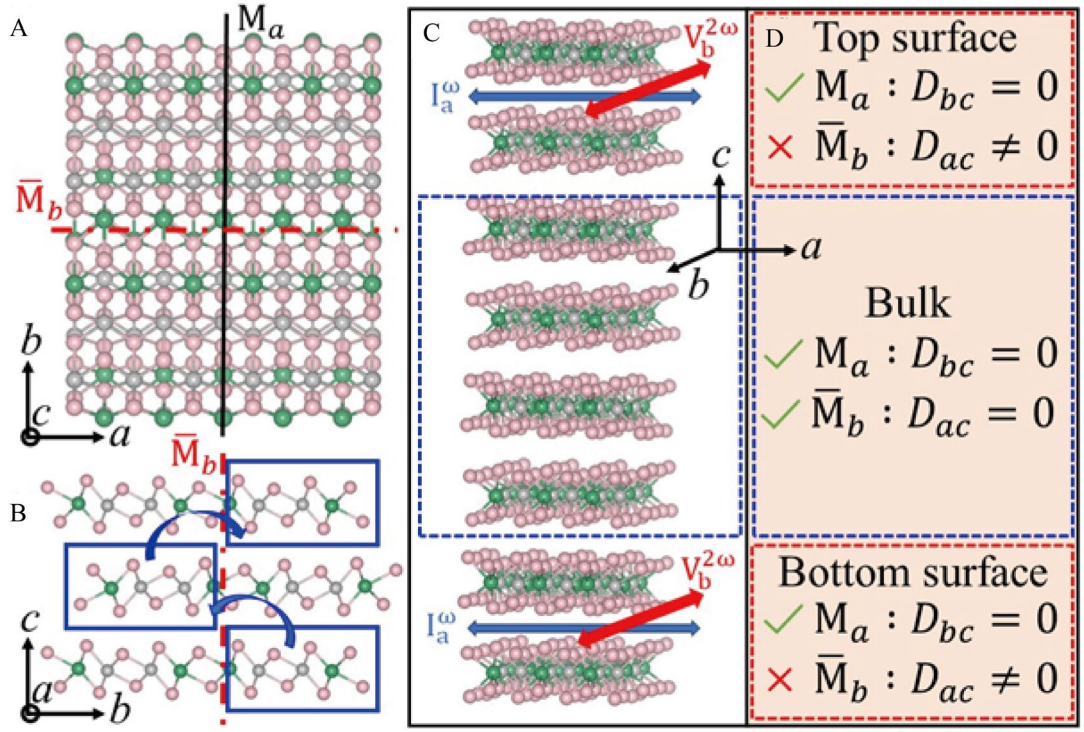

Fig. S5. Crystal structure of $NbIrTe_4$. **(A)** top view, **(B)** side view, and **(C)** 3D view. The mirror plane (M_a) perpendicular to a-axis is clearly visible in top view, and the glide mirror plane ($\bar{M}_b$) perpendicular to ***b***-axis with a translation along ***c***-axis is demonstrated in side view. **D.** Schematic of the contribution of BCD due to the presence /absence of mirror plane symmetry. In bulk, both M_a and $\bar{M}_b$ are present; consequently, the BCD contribution (D_{bc} and D_{ac}) is zero. But, on the surface, glide mirror plane ($\bar{M}_b$) symmetry breaks, consequently NLH response is observed on the surface due to the non-zero BCD contribution, D_{ac}. A second-harmonic Hall voltage response along the b-axis is generated on the surface when an ac is flowing along the ***a***-axis, which is schematically shown in the 3D view.

II.3. Raman spectroscopy of T_d-$NbIrTe_4$

Based on previous research findings, the utilization of angular resolved polarization Raman spectroscopy has been established as a reliable approach to provide evidence for the occurrence of inversion symmetry breaking in both $NbIrTe_4$ bulk crystals and flakes[1]. In line with this, we have also employed Raman spectroscopy to confirm the presence of inversion symmetry breaking in our $NbIrTe_4$ flake. In Fig. S6A, we present the representative Raman spectra obtained from 15 nm thick $NbIrTe_4$ flakes. The observed Raman peaks exhibit excellent agreement with those previously reported in relevant studies[2].

To further our findings and validating the occurrence of inversion symmetry breaking in our $NbIrTe_4$ flake. Angular resolved polarization Raman spectroscopy has been established as a useful technique for determining the crystallographic orientation of $NbIrTe_4$ materials, which exhibit low in-plane crystal symmetry as non-centrosymmetric system materials. Specifically, when the laser's polarization direction is aligned with the crystal axis a, the intensity reaches its maximum at a frequency of approximately 153.6 cm^{-1}. Subsequently, by rotating the polarization direction of the laser counterclockwise by $\theta°$ along the material's crystallographic ***a*** axis to 90°, the Raman spectra of the crystallographic ***a*** and ***b*** axes can be compared, as shown in the Fig. S6B. Crystallographic directions are confirmed via high intensity (***a*** axis) and low intensity (***b*** axis), which is evidence of broken inversion symmstry in $NbIrTe_4$, consistent with previous report. It is worth noting that the peak intensity is strongly dependent on the polarization direction, particularly the 153.6 cm^{-1} mode, as demonstrated in Fig. S6D. Therefore, our $NbIrTe_4$ sample exhibits low symmetry and intrinsic anisotropy, further corroborating our conclusion regarding the presence of inversion symmetry breaking in our $NbIrTe_4$ flake.

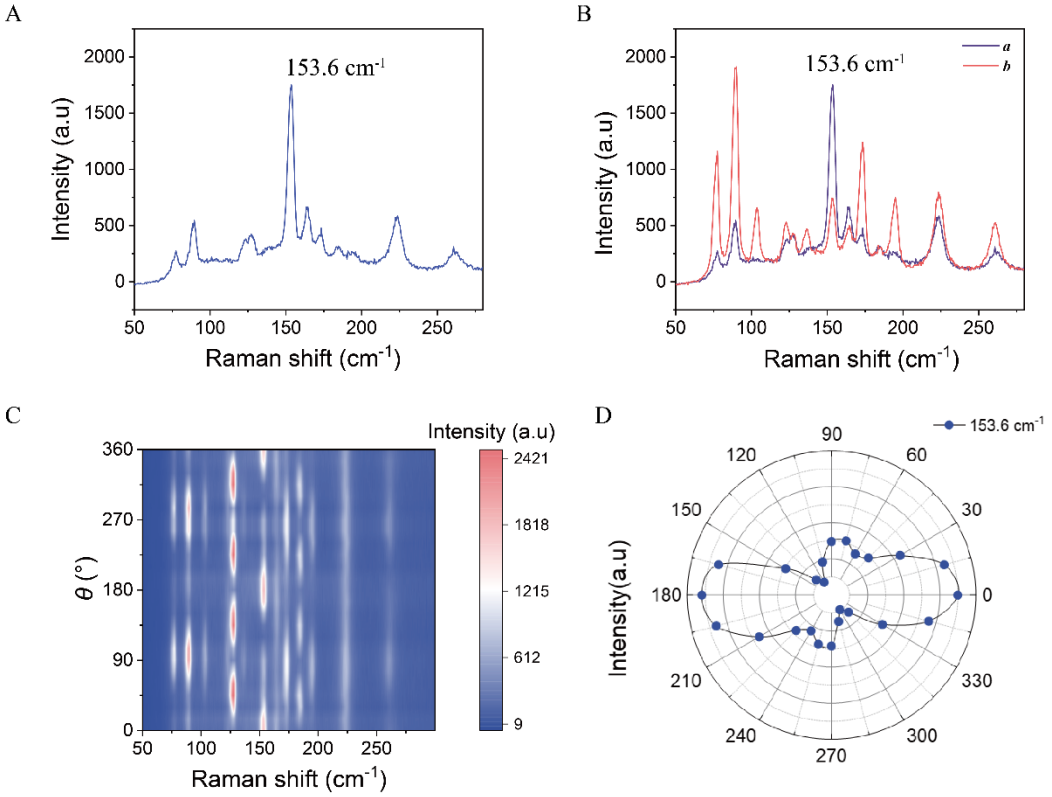

Fig. S6. Raman spectroscopy of T_d-$NbIrTe_4$. **A.** Raman spectrum of multi-layer T_d-$NbIrTe_4$. **B.** Raman spectrum of multi-layer T_d-$NbIrTe_4$ at crystalligraphic axis a and b. The absence of inversion symmstry is revealed, as the clearly anisotropy of axes a and b at the 153.6 cm-1 mode. **C.** Angular resolved Raman spectroscopy of T_d-$NbIrTe_4$ revealing the absence of stronger anisotropy. **D.** Polar plots of Raman modes at 153.6 cm^{-1}. The results are shown asintensity versus angle configuration.

II.4. Optical second harmonic generation of T_d-$NbIrTe_4$

In addition, the analysis of SHG spectra can serve as a means to determine the crystal's low symmetry and crystallographic orientation[3]. In our study, we performed optical SHG measurements on $NbIrTe_4$ samples with varying thicknesses at room temperature, as depicted in Fig. S7A, B. Consistent with the symmetry properties, the strongest SHG signals were observed along the crystallographic ***a***-axis of $NbIrTe_4$. This finding aligns with the results obtained from polarization Raman spectroscopy conducted previously (Fig. S6).

To further investigate the relationship between the incident laser beam's polarization

and the SHG signal intensity, we examined the dependence of the SHG signal intensity on different power levels of the incident laser beam for samples with thin layers, as shown in Fig. S7C. Our data reveals that there is a proportional relationship between the polarization of the incident laser beam and the SHG signal intensity, with a coefficient of 1.79 ± 0.04. This observation provides additional evidence supporting the presence of noncentrosymmetry in our material.

Furthermore, the SHG intensities observed at various thicknesses, as well as the corresponding polarization diagrams, suggest that the material exhibits lower symmetry and more pronounced, stronger SHG signals at thinner thicknesses. This finding is consistent with our subsequent tests on the nonlinear Hall effect, where we observed a greater nonlinear Hall voltage at a thickness of 15 nm.

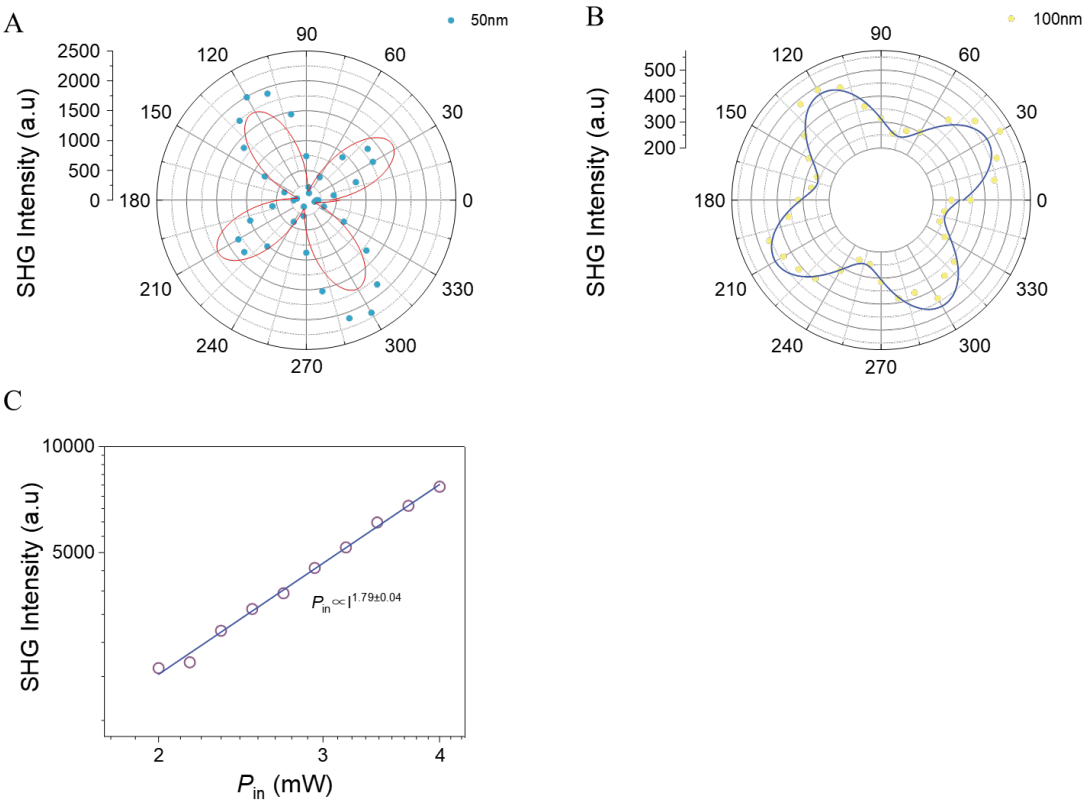

Fig. S7. A-B. Polarization angle dependent SHG for $NbIrTe_4$ samples of various thickness (50 nm and 100 nm). As the material thickness increases, the original symmetry is increasingly broken. **C.** Pump power dependence of intensity of sencond harmonic radiation. The blue line is the result of linear fitting, and the slope is 1.79.

II. 5. Symmetry of Berry curvature (BC) and BCD density, $d_{\alpha\beta} = f(\varepsilon_k - \mu)\frac{\partial \Omega_\beta}{\partial k_\alpha}$

Under mirror symmetry M_a, berry curvature (BC) and BC dipole transform as,

$$\Omega_c(k) = -\Omega_c(-k_a, k_b, k_c),$$

$$d_{ac}(k) = d_{ac}(-k_a, k_b, k_c),\ d_{bc}(k) = -d_{bc}(-k_a, k_b, k_c).$$

Under time-reversal symmetry,

$$\Omega_c(k) = -\Omega_c(-k_a, -k_b, -k_c),$$

$$d_{ac}(k) = d_{ac}(-k_a, -k_b, -k_c),\ d_{bc}(k) = d_{bc}(-k_a, -k_b, -k_c).$$

So, under combined action of time-reversal symmetry and M_a,

$$\Omega_c(k) = \Omega_c(k_a, -k_b, -k_c),$$

$$d_{ac}(k) = d_{ac}(k_a, -k_b, -k_c),\ d_{bc}(k) = -d_{bc}(k_a, -k_b, -k_c).$$

Under glide mirror symmetry $\bar{M}_{\mathrm{b}}$, berry curvature (BC) and BC dipole transform as,

$$\Omega_c(k) = -\Omega_c(k_a, -k_b, k_c + 4\pi/c),$$

$$d_{ac}(k) = -d_{ac}(k_a, -k_b, k_c + 4\pi/c),\ d_{bc}(k) = d_{bc}(k_a, -k_b, k_c + 4\pi/c).$$

So, under combined action of time-reversal symmetry and $\bar{M}_{\mathrm{b}}$,

$$\Omega_c(k) = \Omega_c(-k_a, k_b, -k_c - 4\pi/c),$$

$$d_{ac}(k) = -d_{ac}\left(-k_a, k_b, -k_c - \frac{4\pi}{c}\right), d_{bc}(k) = d_{bc}(-k_a, k_b, -k_c - 4\pi/c)$$

II. 6. Basic transport characterizations

For electrical characterization along the crystallographic direction of $NbIrTe_4$ rectangular thin flakes, we fabricated devices using cross-shaped and standard Hall bar configurations (Fig. S4). Fig. S8 presents the electrical characteristics of a typical Hall bar device. The longitudinal resistivity along the crystallographic ***a***-axis shows typical metallic behavior and saturates below 30 K. Similarly, the resistivity along the ***b***-axis exhibits a comparable trend (Fig. S8A). Moreover, resistivity measurements confirmed the anisotropy of the resistivity along the crystallographic ***a*** and ***b*** axes, as illustrated in Figure S8B. This observation further supports the accuracy of our previous polarization Raman and SHG measurements.

Fig. S8C depicts the relationship between the longitudinal resistivity, Hall resistivity, and out-of-plane magnetic field at 1.7 K. Fig. 8D shows the dependence of ρ_{xy} at ± 9 T from 1.7-300 K. Here, it is evident that the Hall coefficient remains negative at low magnetic field strengths, and the slope of the Hall coefficient decreases as the magnetic field strength increases, indicating a nonlinear trend. As the temperature increases, the slope of the Hall coefficient gradually exhibits a linear trend, suggesting the presence of a multi-band effect in $NbIrTe_4$.

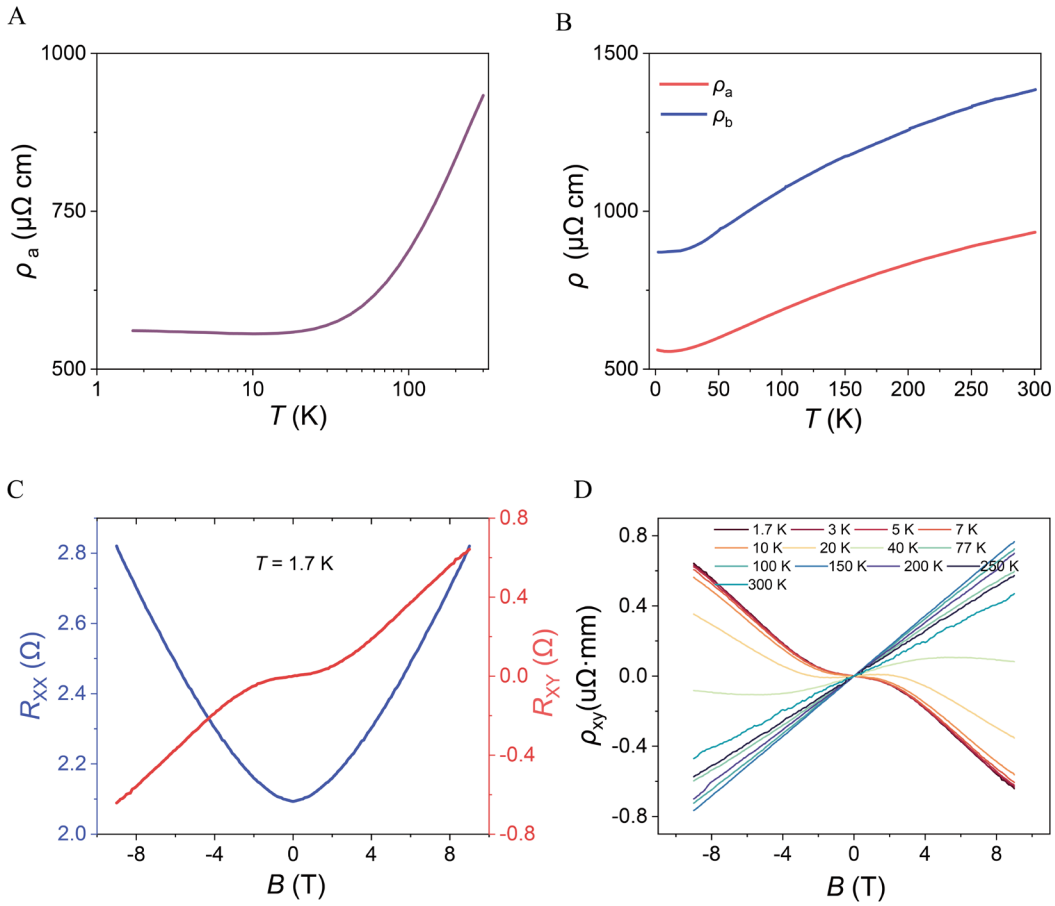

Fig. S8. A. Temperature dependence of the longitudinal resistivity (ρ_a) under zero magnetic field in 15 nm $NbIrTe_4$. **B.** A typical four-probe temperature dependent resistivity (ρ) with current along crystalligraphic a and b axis of 15 nm $NbIrTe_4$. The result shows the anisotropy of the resistivity along the crystallographic ***a*** and ***b*** axes. C. Magnetic field dependence of the longitudinal resistance (R_{xx}) and Hall resistance (R_{xy})at 1.7 K in 15 nm $NbIrTe_4$. D. Magnetic field dependence of the Hall resistivity (ρ_{xy}) at 1.7-300 K.

III. Additional nonlinear transport data

In this section, we unveil supplementary transport data that has not been previously shared. These data carry significant implications in reaffirming our conclusions and deserve careful attention.

III. 1. Frequency-dependence of the nonlinear Hall response

In Fig. S9, we present the frequency-dependent behavior of the nonlinear Hall effect in $NbIrTe_4$ with a thickness of 15 nm. Specifically, Fig. S9A shows the second-order signals of $V_{b-aa}^{2\omega}$ at various frequencies at room temperature, which exhibit consistent behavior. Furthermore, Fig. S9B depicts the persistence of frequency independence even at an increased **a.c** current frequency of 1200 Hz, effectively validates the crucial characteristics of BCD and mitigates potential measurement errors, such as the pseudo-capacitive coupling. In addition, we observe that simultaneous reversal of the current direction and voltage probe electrode leads to a reversal in the sign of the $V_{b-aa}^{2\omega}$.

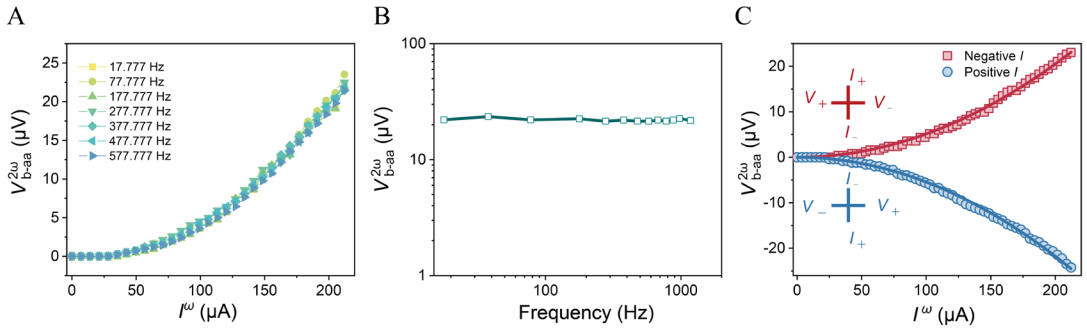

Fig. S9. A. The second-harmonic transverse voltage, $V_{b-aa}^{2\omega}$, with the current along the ***a***-axis for different driving frequencies revealing no frequency dependence of nonlinear Hall voltage. **B.** The nonlinear transverse voltage at different frequencies with a fixed current of I^{ω} =200 μA. **C.** The second-harmonic transverse voltage $V_{b-aa}^{2\omega}$ scales quadratically with the a.c current amplitude I^{ω} in a 15 nm $NbIrTe_4$ at 300 K. A quadratic fit (shown as the solid line) describes the data trend. In the inset, red and blue crossed-geometry illustrate the measurement setup. The current is injected from the source (I^+) electrode to the drain (I^-) electrode, and the voltage is measured between the V^+ and V^- electrodes. As change in sign occurs when both the applied current direction and the corresponding Hall probes are reversed simultaneously.

III. 2. Additional nonlinear Hall data

To validate the precision of the experiment, we replicated it using the standard Hall bar device and multiple cross-geometry devices prepared for $NbIrTe_4$ flakes of varying thickness, as illustrated in Fig. S10A-D. The observation of a room temperature nonlinear Hall effect remained consistent across all these devices.

Additionally, we investigated the temperature dependency of the nonlinear Hall voltage by cooling the 30 nm and 50 nm thickness samples to 2.3 K. Fig.S10E and G displays the linear current-voltage characteristics, indicating ohmic contact behavior in between the device and the material, with a negligible misalignment in the Hall bar geometry leading to the vanishing of $V_{\perp}^{\omega}$. Furthermore, Fig. S10F and H demonstrate that the nonlinear Hall voltage $V_{b-aa}^{2\omega}$ of devices both exhibit the phenomenon of sign reversal, which aligns well with previous reports on $TaIrTe_4$ and confirms the experimental consistency.

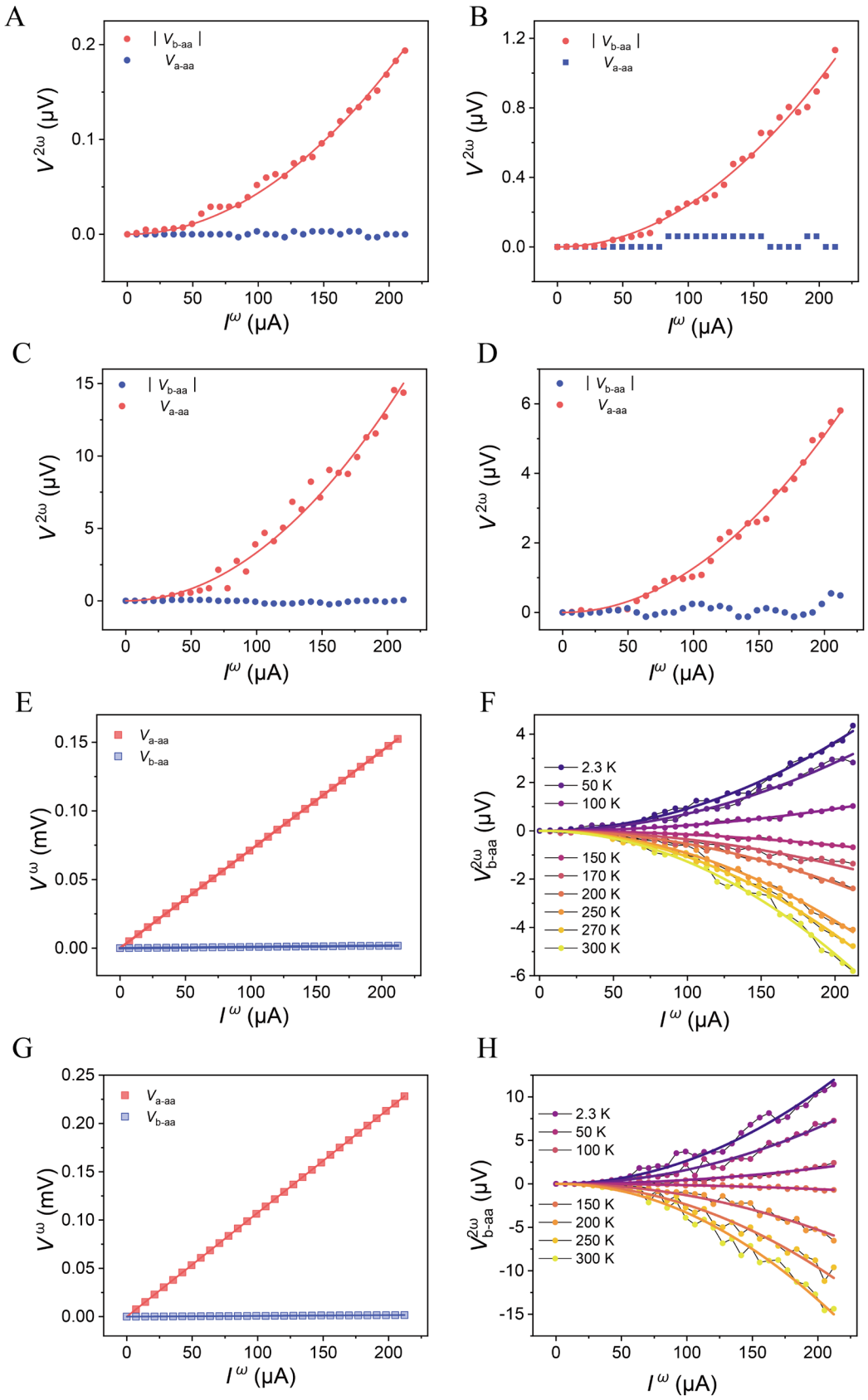

Fig. S10. A-D. The additional data of second harmonic Hall response $V_{b-aa}^{2\omega}$ in $NbIrTe_4$ with various different thickness and geometry configurations. **E, F.** The first harmonic

voltage as a function of the a.c current in 50 nm thick of $NbIrTe_4$. The temperature evolution of $V_{b-aa}^{2\omega}$ across the temperature spectrum of 2.3 - 300 K reveals a change in sign at approximately 130 K. The solid line represents a quadratic fit of the measurements datas. **G, H.** The first harmonic voltage as a function of the a.c current in 25 nm thick of $NbIrTe_4$. The temperature evolution of $V_{b-aa}^{2\omega}$ across the temperature spectrum of 2.3 - 300 K. The solid line represents a quadratic fit of the measurements datas.

III. 3. Observation of room temperature nonlinear Hall effect of non-centrosymmetric $TaIrTe_4$

To investigate the properties of the non-centrosymmetric material system, cross devices and standard Hall rods were fabricated for the previously reported $TaIrTe_4$ material[4]. Fig. S11A illustrates the temperature dependence of the R_{xx} of $TaIrTe_4$. It is evident that this material exhibits typical metallic behavior, approaching a saturation state below 20 K. As with the $NbIrTe_4$ test method, we firstly exerted the current I^{ω} along the ***a***-axis and observed the linear longitudinal voltage (V_{a-aa}^{ω}) and transverse voltage (V_{b-aa}^{ω}), with V_{b-aa}^{ω} sharp smaller than V_{a-aa}^{ω},as shown in top panel of Fig. S11B. This linear current-voltage characteristics, confirming the presence of a typical ohmic behavior, besides a negligible misalignment in the Hall bar geometry from the vanishing of $V_{\perp}^{\omega}$. And observed the nonlinear Hall effect at room temperature, we found a quadratic relationship between $V_{b-aa}^{2\omega}$ and I^{ω}, while $V_{a-aa}^{2\omega}$ was significantly smaller than $V_{b-aa}^{2\omega}$, confirming the second-order nature of the interesting “Hall dominance” in $TaIrTe_4$. Subsequently, a frequency-dependent experiment on the nonlinear Hall voltage signal was conducted, revealing its lack of frequency dependence (Fig. S11C). These characteristics are generally in line with $NbIrTe_4$ and the previously reported $TaIrTe_4$[4].

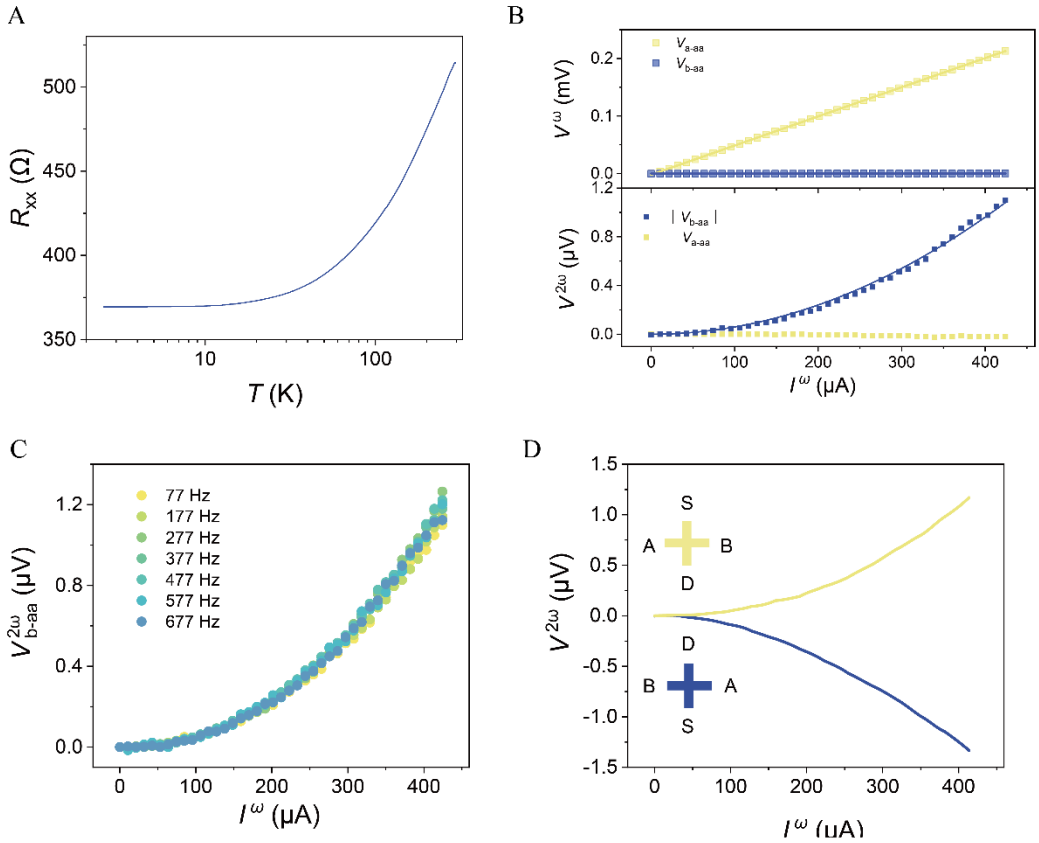

Fig. S11. A. Temperature dependence of the longitudinal resistance (R_{xx}) under zero magnetic field in 50 nm $TaIrTe_4$. **B.** The longitudinal and transverse first-harmonic and second-harmonic voltage as a function of a.c. current amplitude I^{ω}. **C.** The nonlinear longitudinal voltage as a quadratic function of applied current across varying frequencies. **D.** The second-harmonic transverse voltage $V^{2\omega}$ scales quadratically with the a.c current amplitude I^{ω} in a 50 nm $TaIrTe_4$ at 300 K. In the inset, red and blue crossed-geometry illustrate the measurement setup. The current is injected from the source (S) electrode to the drain (D) electrode, and the voltage is measured between the A and B electrodes. As change in sign occurs when both the applied current direction and the corresponding Hall probes are reversed simultaneously.

IV. Addressing alternative mechanisms for the nonlinear Hall signals

Here, we comprehensively enumerate the potential external influences and meticulously analyze each one in detail.

1. Thermoelectric effect due to Joule heating:

It is well-established that Joule heating induces a temperature gradient (ΔT) within the sample, which consequently generates a thermoelectric voltage ($V_{TE} \propto I^2R$) [5]. As joule heating is influenced by external factors such as contact resistance and sample geometry, the thermoelectric signal V_{TE} is not intrinsically sensitive to crystal orientation. Consequently, one would anticipate that the transverse thermoelectric response would not surpass the longitudinal thermoelectric response. However, our experimental data intriguingly reveal that $V_{b-aa}^{2\omega}$. exhibits a Hall dominance, defying conventional expectations.

2. Contact junctions:

The presence of an unforeseen diode-like behavior at the interface between the material and the electrode could potentially introduce a rectification effect. However, we can confidently exclude the contribution of any nonlinear signal produced by this diode based on the following observations: (1) The nonlinear Hall voltage $V_{b-aa}^{2\omega}$ displays a reversal in sign during the cooling process, indicating that it is not solely attributable to the diode-like behavior. (2) The nonlinear Hall voltage $V_{b-aa}^{2\omega}$ exhibits a prominent Hall dominance, further supporting the notion that it is not solely a result of the rectification effect. (3) The linear current-voltage (I-V) characteristics of numerous devices suggest that there is excellent ohmic contact within the system, thereby minimizing any potential influence from the diode-like behavior.

3. Flake shape:

The shape asymmetry of the sample introduces an additional external influence. This is because the asymmetry in the sample's overall shape can result in carrier collisions with the asymmetric boundary, leading to nonequilibrium carrier motion and the potential generation of a nonlinear signal.

However, we have carefully considered this possibility and have compelling reasons to exclude the contribution of any deformation-induced nonlinear signal:

(1) To minimize the error caused by large deformations, the rectangular $NbIrTe_4$ material undergoes precise etching using FIB techniques to achieve a regular cross or standard Hall bar shape during the device preparation process.

(2) The observed nonlinear Hall signal $V_{b-aa}^{2\omega}$ exhibits clear Hall dominance and is prohibited when the current is applied along the mirror M_a direction. This further supports the conclusion that any nonlinear signal arising from deformation effects is negligible.

(3) We have noted that the nonlinear Hall signal strongly depends on temperature and carrier density, demonstrating sign inversion during temperature changes. This behavior suggests that the nonlinear signal primarily originates from intrinsic electronic properties rather than external factors such as sample deformation.

V. The potential contributions and scaling laws of nonlinear Hall conductivity.

In this section, we begin by exploring the various potential contributions that may lead to nonlinear Hall conductivity, along with the corresponding dependencies of nonlinear Hall conductivity on scattering time τ. This approach offers a direct pathway to uncovering the microscopic mechanisms responsible for generating the nonlinear Hall effect through scaling analysis. Lastly, by scrutinizing the scaling laws of nonlinear conductivity, we aim to clarify the origins of the observed nonlinear Hall effect in NbIrTe4 within our experimental framework.

V. 1. The influence of disorder and other mechanism on nonlinear Hall response in $NbIrTe_4$

For the nonlinear Hall effect, which follows a τ^2-order, it is primarily governed by nonlinear Drude transport weight term:

$$\sigma_{\alpha\beta\gamma}^{(2)Drude} = \frac{-\tau^2 e^3}{\hbar^3} \sum_n \int dk \left(\partial_{k_\alpha} \partial_{k_\beta} \partial_{k_\gamma} \epsilon_n(k)\right) f_n$$

In contrast, the terms to NLHE proportional to τ^1-order include such as geometric components BCD ($\sigma_{\alpha\beta\gamma}^{BCD} = \frac{e^3\tau}{\hbar^2} \epsilon_{\alpha\beta\gamma} D_{\gamma\delta}$, where - e is the elementary charge, $\epsilon_{\alpha\beta\gamma}$ is the antisymmetric Levi-Civita tensor, $f_n$is the Fermi-Dirac distribution for band n, $D_{\gamma\delta}$ is

the BCD), side jumps $\sigma_{\alpha\beta\gamma}^{sj}$, as well as intrinsic and extrinsic skew scattering ($\sigma_{\alpha\beta\gamma}^{sk,1}$ and $\sigma_{\alpha\beta\gamma}^{sk,2}$). Additionally, besides the quantum metric $g_{\alpha\beta}$, there are 2nd-order side jumps and skew scattering terms related to τ^0-order, which have been validated in numerous previous studies[6-11].

In addition, we compile a table summarizing how different mechanisms generate the nonlinear Hall effect, detailing their corresponding dependencies of nonlinear Hall conductivity on scattering time (τ) under various symmetries. This will be presented in Table S1.

Table S1| Summary of the scattering time τ dependence, the symmetry analysis, and longitudinal ($J_{\parallel}$) and transverse ($J_{\perp}$) currents for different mechanism (✗ means forbidden by symmetry, "✓" means allowed by symmetry, * denotes this work).

Mechanism	τ-dependence	Symmestry			$J_{\perp}$	$J_{//}$
		P	T	PT		
Berry curvature dipole (9) *	τ^1	✗	✓	✗	✓	✗
Skew scattering (18,42)	τ^3or τ^2	✗	✓	✗	✓	✗
Side jump (18)	τ^2or τ^1	✗	✓	✗	✓	✗
Anomalous skew scattering (60)	τ^2	✗	✗	✓	✓	✗
Second order Drude term (61)	τ^2	✗	✗	✓	✓	✓
Quantum metric dipole (22, 23)	τ^0	✗	✗	✓	✓	✓

V.2 Scaling law of nonlinear Hall conductivity in $NbIrTe_4$

The relation between the intensity of the nonlinear Hall effect to resistivity was established by Du et al[7]. Thus, taking into account the connection between $\frac{E_{b-aa}^{2w}}{(E_{a-aa})^2}$ and the conductivity σ_{aa}, the scaling law for the nonlinear conductivity observed in our experiments can be formulated as follows:

$$\frac{E_{b-aa}^{2w}}{(E_{a-aa})^2} = C_1\sigma_{aa0}^{-1}\sigma_{aa}^{2} + (C_2 - C_3 + C_4)\sigma_{aa0}^{-2}\sigma_{aa}^{2} + (C_3 - 2C_4)\sigma_{aa0}^{-1}\sigma_{aa}^{1} + C_4 \qquad \text{(S1)}$$

Including four scaling parameters:

$$C_1 = C^{sk}, C_2 = C^{in} + C_0^{\mathrm{sj}} + C_{00}^{sj},$$

$$C_3 = 2C^{in} + C_0^{\mathrm{sj}} + C_1^{\mathrm{sj}} + C_{01}^{sj}, \quad \text{(S2)}$$

$$C_4 = C^{in} + C_1^{\mathrm{sj}} + C_{11}^{sj}.$$

Here, σ_{aa} denotes the conductivity along the a-axis, with, σ_{aa0} representing the residual conductivity due to static impurities at zero temperature. σ_{aaT}=ρ_{aaT}^{-1}≡$(\rho_{aa} - \rho_{aa0})^{-1}$ signifies the residual conductivity induced by dynamic scattering, such as phonon scattering, at finite temperatures. $C_{1,2,3,4}$ correspond to contributions from intrinsic, skew, intrinsic-skew, and external-skew scattering sources, where indices (i, j) denote different scattering mechanisms—considering both static (i, j = 0) and dynamic (i, j = 1). Thus, we express this in terms of the experimental variable σ_{aa}:

$$\frac{E_{b-aa}^{2w}}{(E_{a-aa})^2} = \xi\sigma_{aa}^2 + \zeta\sigma_{aa} + \eta \quad \text{(S3)}$$

Where,

$$\eta = C_4 = C^{in} + C_1^{\mathrm{sj}} + C_{11}^{sj},$$

$$\zeta = (C_3 - 2C_4)\sigma_{aa0}^{-1} = (C_0^{\mathrm{sj}} + C_{01}^{sj} - C_1^{\mathrm{sj}} - 2C_{11}^{sj})\sigma_{aa0}^{-1} \quad \text{(S4)}$$

$$\xi = C_1\sigma_{aa0}^{-1} + (C_2 - C_3 + C_4)\sigma_{aa0}^{-2} = C^{sj}\,\sigma_{aa0}^{-1} + (C_{00}^{sj} - C_{01}^{sj} + C_{11}^{sj})\sigma_{aa0}^{-2}$$

It is noteworthy that in the actual analysis of data concerning nonlinear Hall conductivity, as depicted above (S2), we do not specifically address the identification of asymmetric contributions in semiclassical processes, such as lateral or oblique scattering rates[12]. Moreover, according to semiclassical theory, the collective contribution of all asymmetric scattering rates present in the collision term of the Boltzmann transport equation is termed intrinsic oblique scattering[7]. However, in our definition (S2), this contribution is not categorized as oblique scattering but is instead subsumed under the framework of side scattering (sj), as per previous comprehensive studies on multivariable scale transport effects[12].

Table S2| The scaling laws of the nonlinear conductivity. It reveals the coefficients η, ζ, and ξ for device thicknesses of 15 nm, 25 nm, and 50 nm, derived from fitting equation (3).

Thickness	η (10^{-8} m V^{-1})	ξ (10^{-13} m^3 V^{-1} S^{-1})	ξ (10^{-18} m^3V^{-1} S^{-2})
15 nm	−1.48±0.03	0.7±0.02	0
15 nm	-1.22±0.27	0.47±0.25	0.051±0.05
25 nm	-0.49±0.04	0	0.18±0.01
25 nm	0.12±0.22	-0.68±0.25	0.36±0.07
50 nm	1.33±2.3	-5.67±3.39	3.43±1.22
50 nm	-2.51±0.16	0	1.4±0.08

According to the results in Table S2, it is evident that when the device thickness is 15 nm, the static scattering ζ is significantly smaller than the contributions from intrinsic (Berry curvature dipole) and dynamic disorder scattering. This linear scaling behavior of ζ is also observed in thin WTe_2 and $TaIrTe_4$[4,8]. Intriguingly, we find that the scaling behavior deviates from being linear as conductivity decreases, with the parabolic term becoming dominant，as predicted by Du et al[7].

VI. The model describes the generation of frequency comb harmonics by high-order nonlinear effects.

The high-harmonic generation (HHG) in bulk materials arises from the combined effects of intraband and interband transitions manifesting in the nonlinear current[13-17]. The intraband contribution is a result of nonlinear currents caused by non-parabolic band dispersion, while the interband contribution occurs due to an induced polarization between the valence and conduction bands. The presence of even harmonics in $NbIrTe_4$ is attributed to a finite Berry curvature. To gain insight into the origin of the even harmonics, we provide a simple and intuitive model based on semiclassical dynamics within a single band that qualitatively captures the main features of our measurement. In order for this model to be true, it is necessary for the electron to move across a significant portion of the Brillouin zone within a short period of time, relative to interband transitions. This means that the Bloch frequency must be considerably higher than the required Rabi frequency. Within this limit, we demonstrate that the semiclassical equations governing the intraband current, with the inclusion of the Berry

curvature contribution, can generate odd and even harmonics. These harmonics are polarized in parallel and perpendicular directions to the driving field, respectively. The k-dependent group velocity, according to the semiclassical equation of motion, can be expressed as,

$$v_n(k(t)) = \frac{1}{\hbar}\frac{\partial \varepsilon_n(k)}{\partial k} - \frac{e}{\hbar}E(t) \times \Omega_n(\mathbf{k}) = v_{||}(t) + v_{\perp}(t)\,.$$

Here, $\mathbf{E}$(t), $\varepsilon_n(k)$, $\Omega_n(\mathbf{k})$ are the electric field, band dispersion, and Berry curvature of the n-th band. The first term generates odd harmonics polarized parallel to the driving electric field, while the anomalous velocity induced second term generates even harmonics perpendicular to the electric field. The associated high-harmonic (HH) spectrum of the non-linear intraband current can be calculated as proportional to $|FT[v_n(t)]|^2$, where FT denotes the Fourier transform.

The odd-order high harmonic generation (HHG) arises from the nonlinear acceleration of electrons in the electronic band structure, as dictated by the intraband Bloch oscillation mechanisms. The electronic band dispersion can be expressed as, $\varepsilon_n(k) = \sum_{p=0}^{p_{max}} \epsilon_{n,p}\, cos(pka)$, where n, k, and a are the band index, the Bloch wavevector and the lattice constant, respectively. The presence time-reversal symmetry in $NbIrTe_4$ makes $\varepsilon_n(k)$ an even function of wavevector k, yielding only cosine terms. The intensity of odd-order HHG is given by ref. [13],

$$I_{n,2m-1} \propto \left| FT\left\{ \sum_{p=0}^{p_{max}} na\epsilon_{n,p}\, J_{2m-1}(n\frac{\omega_B}{\omega_L})\, cos\,[(2m-1)\omega_L t] \right\} \right|^2.$$

Here, ω_L and $\omega_B = \frac{eE_0 a}{\hbar}$ are the frequency of the fundamental wave and the Bloch frequency, E_0 is the amplitude of the fundamental wave and J_{2m-1} is the (2m-1) order Bessel function of first kind.

The intensity of even-order HHG is given by [13],

$$I_{n,2m} \propto \left| FT\left\{ \sum_{p=0}^{p_{max}} \frac{\omega_B}{a}\gamma_{n,p}\, J_{2m-1}(n\frac{\omega_B}{\omega_L})\, \{sin\,[2m\omega_L t] + sin\,[(2m-2)\omega_L t]\} \right\} \right|^2,$$

where $\gamma_{n,p}$ is the p-order expansion coefficient of Berry curvature of n-th band in reciprocal space. The BC can be expressed as, $\Omega_n(k) = \sum_{p=0}^{p_{max}} \epsilon_{n,p}\, sin(pka)$. Here

there are only sine functions in the BC expression, as $\Omega_n(k)$ is odd-function of wavevector k under the time-reversal-symmetry.

The calculated HHG spectrum of $NbIrTe_4$ is depicted in Fig. S12, where we clearly observe both odd and even harmonics, corroborating the experimental findings. In the strong-field limit, perpendicularly polarized even harmonics can arise due to the unique non-zero Berry curvature along ***a***-axis as a result of the broken inversion symmetry, as illustrated by the model given above, which provides a straightforward and intuitive depiction of the HHG process.

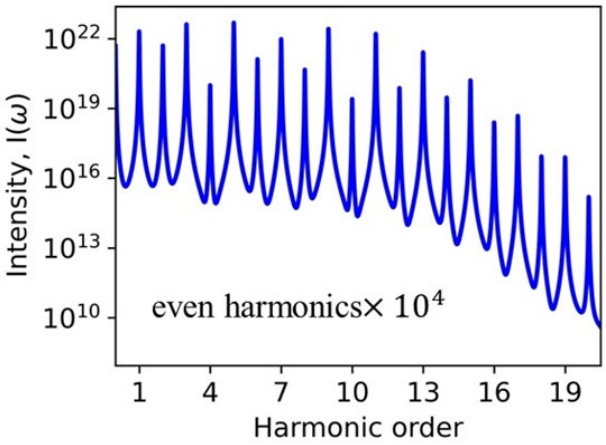

Fig. S12. Calculated HHG spectrum of $NbIrTe_4$. Odd and even harmonics in the semiclassical model for an incident linearly polarized light.

VII. Additional data of frequency-comb and mixing frequency in $NbIrTe_4$ Hall mixer

In this section, we provide additional data on the frequency comb and mixing frequency of $NbIrTe_4$ mixer in the RF band that has not been included in the main text. These data are crucial to validate our conclusions and the reproducibility of the experimental results.

VII. 1. Frequency-comb at different f_{LO} in $NbIrTe_4$ Hall mixer

As shown in the experimental setup depicted in Fig. 3c of the main text, we directly feed the LO signal through an SubMiniature version A connector (SMA) connection to the ***a***-axis of the crossed-geometry device, as illustrated in Fig. S4A, which shows the raw data of the frequency comb recovered by a spectrum analyzer. It can be observed

that when the LO signal with f_{LO} = 1 GHz is input to the ***a***-axis of the crossed-geometry device, the spectrum analyzer connected to the ***b***-axis detects frequency comb harmonics up to the 27th order (setup limited). However, as the same input is applied to the ***b***-axis of the crossed-geometry device, the output signal of the ***a***-axis significantly samller than the output magnitude of ***b***-axis, and higher comb orders essentially vanish. This confirms the dominance of the frequency comb in $NbIrTe_4$. More importantly, it can be concluded that the origin of our frequency comb generation: The odd-order high harmonic generation (HHG) arises from the nonlinear acceleration of electrons dictated by the longitudinal intraband Bloch oscillation induced by the band velocity. The even-order high harmonics originate from the transverse Bloch oscillations arising from the non-zero Berry curvature (presence of $\overline{M}_b$ symmetry)[13,15]. Additionally, as shown in Fig. S13B, D, F, the scaling ralationship between input power and output power clearly suggests the non-perturbative nature of freuqency comb generation in the $NbIrTe_4$. Furthermore, similar results are observed for inputs at f_{LO} = 1.5, 6, 8, and 10 GHz, corresponding to Figs. S12C-H. These findings consistently indicate that our approach provides an alternative strategy for generating high-frequency microwaves/millimeter waves.

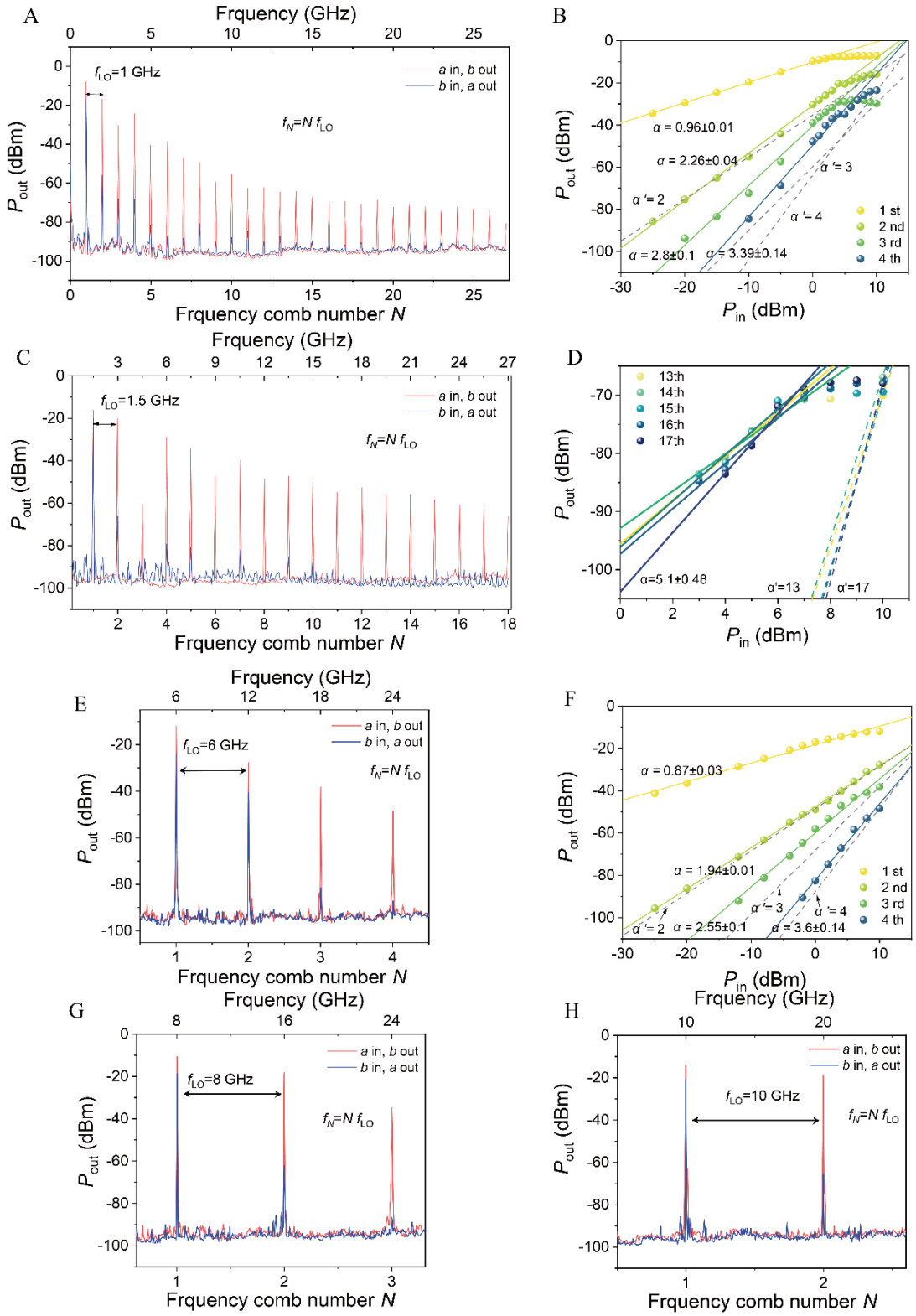

Fig. S13. A-H. The frequency comb line for different LO inputs (f_{LO}=1, 1.5, 6, 8, 10 GHz), with frequency comb number ***N*** of 27, 17, 4, 3, 2, respectively. **B, D, F.** The scaling relationship between the power of higher-order harmonic-frequency and fundamental input-signal (f_{LO}=1, 1.5, 6 GHz). The solid line is a linear fitting of the

measurements, while the dashed line marks a linear fit of non-perturbation.

VII. 2. Wave-mixing at different f_{LO} and f_{RF} in other $NbIrTe_4$ Hall mixer

In this main text, we apply f_{LO} and frf of 21, 24 GHz, respectively. Here, we apply f_{LO} and f_{RF} of 10.4, 13 GHz, respectively. The experimental setup is shown in Fig. S14A. The experimental process has been mentioned in the main text and is not repeated here. After the experiment, following the power-scaling rule, the output power of different subharmonic mixing is fitted with the equation $P_{out} = \alpha P_{in}$ ($P_{in}=P_{fLO}$, P_{fRF}). The fitting results are depicted in Fig. 3f and 3g respectively, with the dashed line labeling the traditional dependence of perturbed nonlinear optics[18]. and the solid line representing the slope of the output power P_{out} measured from the experiment. The power dependence strongly suggests the nonperturbative nature of the subharmonic mixing or N-wave mixing process in $NbIrTe_4$. Our results confirm the emergence of 3-wave ($2f_{RF}$) and 12-wave ($6f_{RF}$-$5f_{LO}$) mixing at 26 GHz, 3-wave (f_{LO}+f_{RF}) and 10-wave ($5f_{RF}$-$4f_{LO}$) mixing peaks at 23.4 GHz, 3-wave ($2f_{LO}$) and 8-wave ($4f_{RF}$-$3f_{LO}$) mixing peaks at 20.8 GHz, 6-wave ($3f_{LO}$- $2f_{RF}$) and 15-wave ($7(f_{RF}$-$f_{LO})$) mixing peaks at 18.2 GHz, 4-wave ($2f_{LO}$- f_{RF}) and 7wave ($3(f_{RF}$-$f_{LO})$) mixing peaks at 7.8 GHz, 5-wave ($2f_{RF}$-f_{LO}) and 6wave ($3f_{LO}$-$2f_{RF}$) mixing peaks at 5.2 GHz,and 3-wave mixing (f_{RF}-$f_{LO)}$ at 2.6 GHz, consistent well with the theoretical framework. Remarkably, even under the lower limit of RF input within our setup (P_{RF}=-25 dBm, P_{LO}=14.8 dBm), it can clearly identify the generation of 3-, 4-, and 7-WM signals. Thus, it represents that the border of low-power excitation threshold is less than -25 dBm, manifesting the promising prospect of the NLHE device for acquiring precise carrier-frequency information and long-distance data preprocessing.

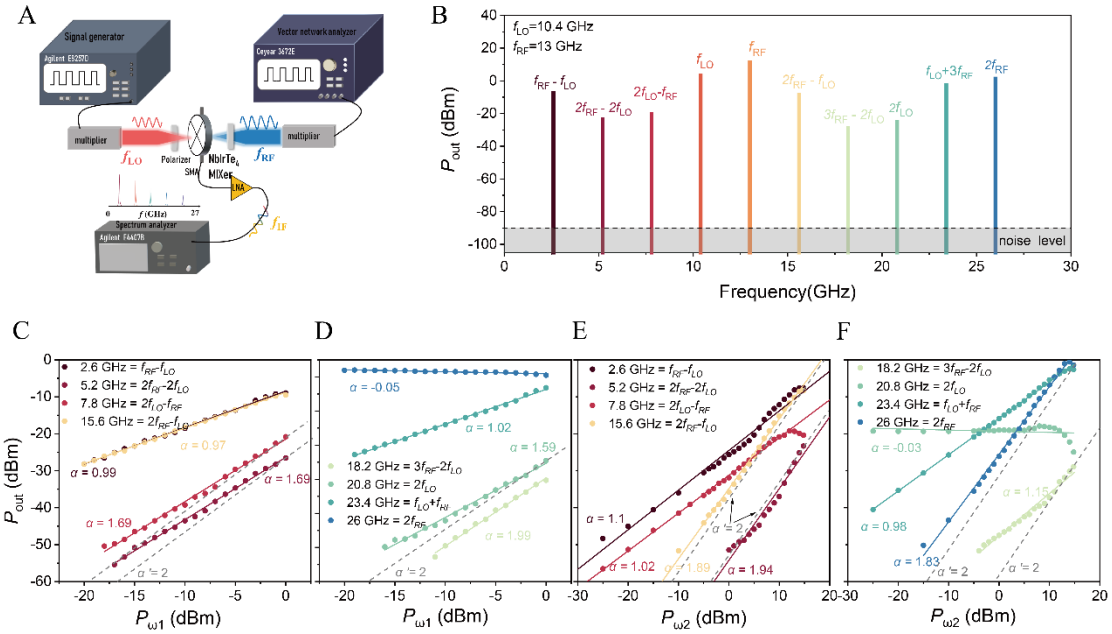

Fig. S14. A. The experimental setup for wave-mixing frequency in radio frequency band. **B.** The mixing frequency spectrum is recorded by a spectrum analyzer at room temperature when the input LO signal. f_{LO} is set to 21 GHz and f_{RF} is 24 GHz. Each peak value is indicated in the figure. **C-F.** These diagrams depict the scaling relationship between the input power of fundamental order (f_{LO} and f_{RF}) and output power of N-wave mixing signal measured experimentally, respectively. The dashed line (α') represents linear fitting of non-perturbation. The solid line (α) is a linear fitting of the measurements.

VII. 3. Heterodyney mixing in the terahertz band based on $NbIrTe_4$ mixers

To showcase the exceptional high-frequency capabilities inherent in our $NbIrTe_4$-based mixer, we have embarked on extending the heterodyne mixing range well into the terahertz spectrum. This necessitated adjusting the LO frequency to exceed 100 GHz, as depicted in Fig. S15A, while RF frequencies are tuned to range from the Ku, Ka, to W bands. Meanwhile, we extracted the experimental data and caltulated the conversion loss of the entire wideband LO signal, as depicted in Figure S15B, which ranging from approximately 10 to 75 dB.

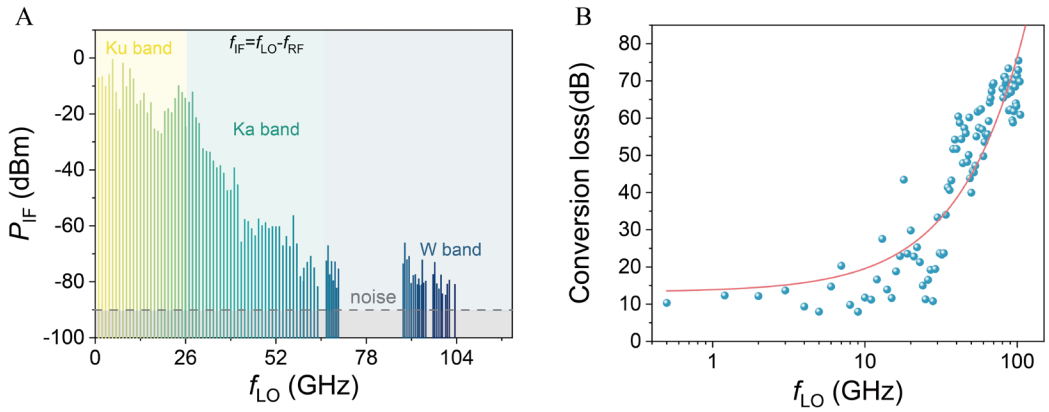

Fig. S15. A. The spectrum of the IF output power signal as the LO frequency varies in a heterodyne mixer setup. Here, the IF output signal frequency is $f_{IF}= f_{LO} - f_{RF}$, RF frequency covering the bands Ku, Ka, and W. **B.** Calculated conversion loss (*CL*) as a function of LO frequency [19].

VII. 4. Power-scaling rule for multi-subharmonic mixing at different harmonic order *N*

By incorporating this broadband frequency comb as a LO source, the required burden of high-frequency and wide-band LO source is effectively reduced and the radio frequency bandwidth of heterodyne receiver can be increased to unprecedented level. Therefore, to validate the practical application of RF frequency comb generation, we demonstrate multi-subharmonic mixing harnessing its intrinsic capabilities of the $NbIrTe_4$ device. As shown in Fig. S16A-E, the heterodyne mixing frequency spectra display harmonics of each local frequency [19] and a fixed RF (f_{RF}), where f_{LO} corresponds to 45.4, 27, 22, 18, 14.5 GHz respectively. This result demonstrates the practical application of our frequency comb, effectively reducing the requirement for a high-frequency wideband local oscillator source. It is noteworthy that in the perturbative limit, the following correlations should be observed between the IF output power and the LO input power raised to the Nth power:

$$P_{out} \propto P_{in}^{\alpha}$$

$$\log(P_{out}) \propto \alpha \, log(P_{in}) + P_0$$

As shown in Fig. S16F-J, the scaling laws of higher harmonic orders differ markedly from those of traditional perturbative nonlinear optics (e.g., in $5f_{LO}$-f_{RF}, α should exhibit a slope indicating a power dependence of 5 in the perturbative limit). Therefore, the clear power-dependent scaling rates indicate that the high harmonic mixing process in $NbIrTe_4$ is non-perturbative in nature. Moreover, this non-perturbative nonlinearity can simultaneously generate odd and even harmonics, thereby reaffirming our conclusion: The odd-order high harmonic generation (HHG) arises from the nonlinear acceleration of electrons dictated by the longitudinal intraband Bloch oscillation induced by the band velocity. The even-order high harmonics originate from the transverse Bloch oscillations arising from the non-zero Berry curvature.

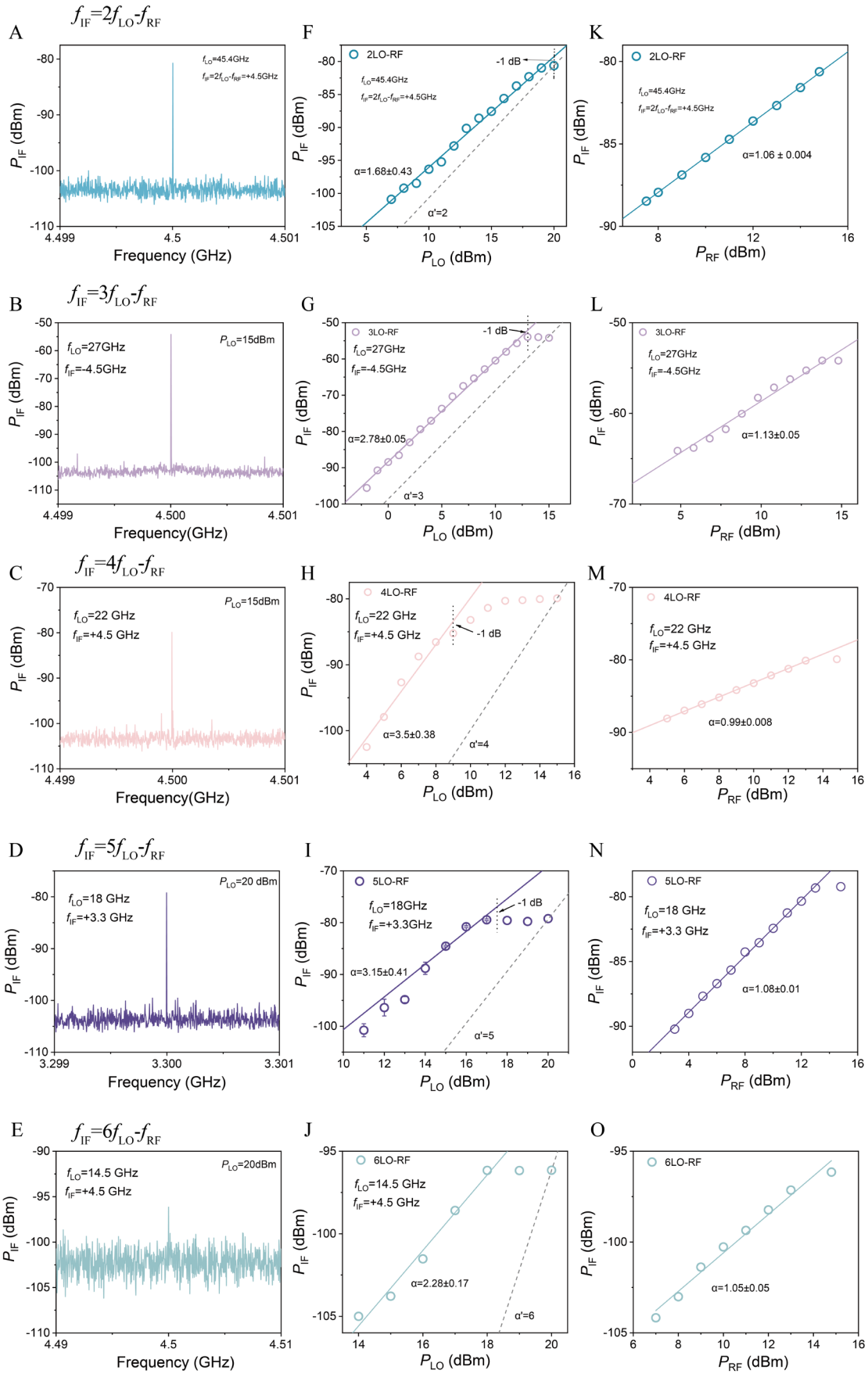

Fig. S16. A-E. These spectra represent intermediate frequency signals in the multi-

subharmonic heterodyne mixing (f_{IF}=nf_{LO} - f_{RF}, where n is 2, 3, 4, 5, 6), with f_{LO} corresponding to 45.4, 27, 22, 18, 14.5 GHz, respectively. **F-J.** The scaling relationship between the power of higher-order harmonic-frequency (2, 3, 4, 5, 6-order) and fundamental input-signal (45.4, 27, 22, 18, 14.5 GHz). The solid line is a linear fitting of the measurements, while the dashed line marks a linear fit of perturbation with a fixed slope between 2 and 6, respectively. The 1 dB compression point is marked by black arrow. **K-Q.** The scaling relationship between the output power of radio frequency (f_{RF}) and its input.

VIII. Additional data of $NbIrTe_4$ THz Hall rectifier

In this section, we supplement the specific data on terahertz rectifiers not shared in the text. These data are important for reaffirming our conclusions and deserve careful attention.

VIII. 1. Terahertz detection of the T_d- $NbIrTe_4$ Hall rectifier

Next, we harness the observed room-temperature nonlinear Hall effect in $NbIrTe_4$ to demonstrate terahertz band rectification, achieved without bias or magnetic fields. This second-order phenomenon introduces an innovative method of converting oscillating electromagnetic fields into direct current, thereby harvesting electromagnetic energy. Fig. 4i illustrates the conceptual diagram of rectification, while the experimental device configuration is detailed in Fig. S17A. In a process akin to measuring nonlinear second harmonics, we align the incident terahertz field E^{ω} along the ***a***-axis and measure the resulting DC current along the ***b***-axis. Fig. S17B, C present DC signals spanning 0.025-0.12 THz. Notably, when E^{ω} aligns with the ***b***-axis, in accordance with NLHE symmetry constraints, the measured current j_{a-bb}^{DC} is clearly smaller than j_{b-aa}^{DC}, as depicted in Fig. S17D, E. Further exploration involves polarizer angle variation, revealing maximum transverse photocurrent polarization at θ=0° angle, with response peaks observed at 0.034 and 0.103 THz, detailed in Fig. S17D, E.

Additionally, we theoretically calculate the polarization angle dependence of the BCD

and $j_{\theta}^{2\omega}$, as shown in Fig. S17F and G. The results are also consistent with the mechanisms underlying the generation of frequency comb and nonlinear Hall response in the T_d-$NbIrTe_4$, predominantly arise from the Berry curvature dipole. Furthermore, our rectifier exhibits robust responses at frequencies including 0.278, 0.443, 0.490, 0.540, 0.740, and 0.820 THz, although rectification signals diminish at higher frequencies, accompanied by minor time domain waveform distortion.

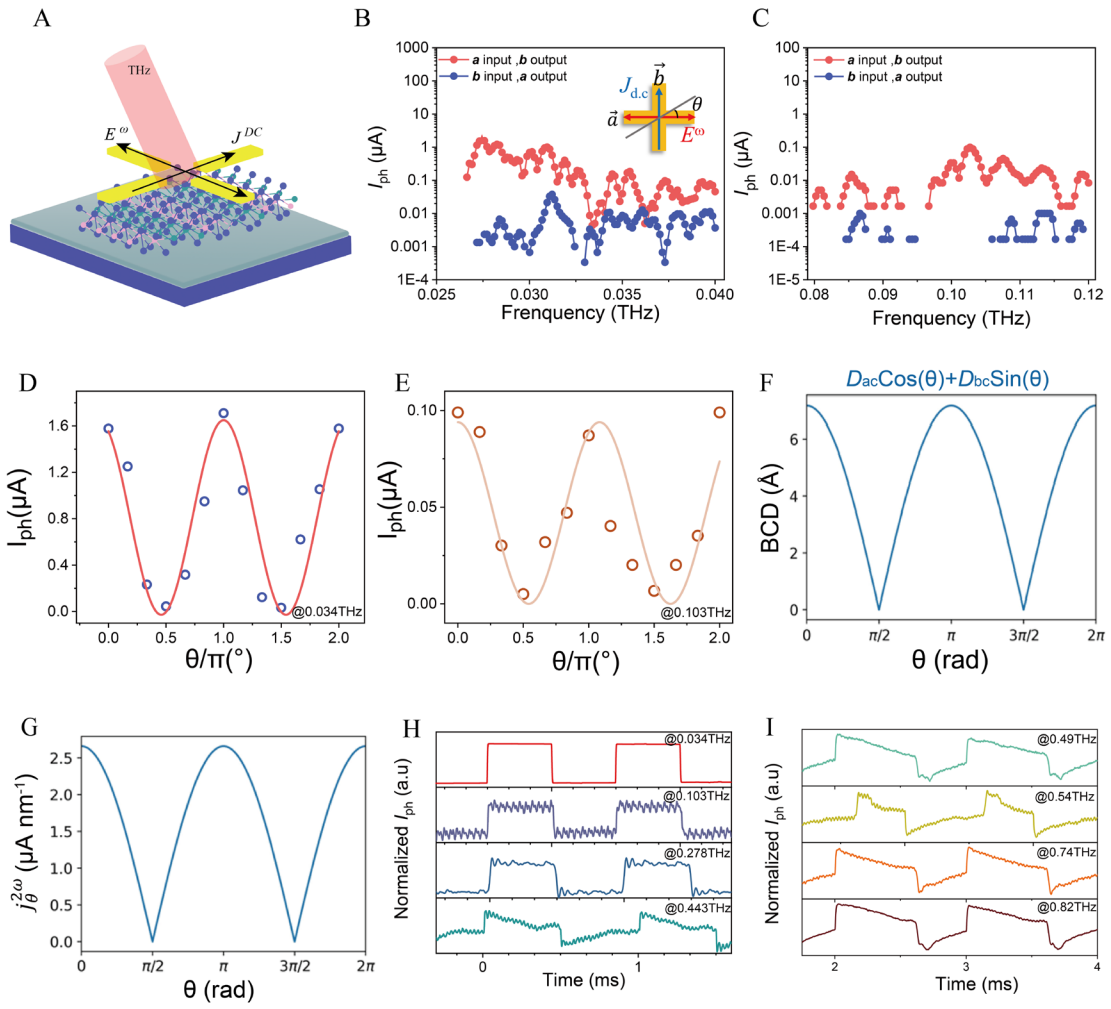

Fig. S17. Terahertz detection of $NbIrTe_4$-based nonlinear Hall rectifier. A. Schematic of the device made from crossed-geometry. The oscillating terahertz electric field enhanced by the antenna induces a direct current in the transverse direction via the second-order nonlinear Hall response. **B, C**. The spectral dependence of the measured rectified photocurrent is obtained when the terahertz field is along the antenna ($\theta = 0°$). The inset shows the experimental geometry. Spectral frequency in 0.02–0.04 THz for **(B)**, in 0.08–0.12 THz for **(C)**. **D, E.** The maximum transverse photocurrent polarization

dependence occurs at a polarization angle θ = 0°. The peak frequencies of specific polarized optical currents are **(D)** 0.027 THz and **(E)** 0.103 THz respectively. **F, G.** Theoretically calculated angular dependence of **(F)** BCD and **(G)** non-linear Hall current density, $J_{\theta}^{2\omega}$. $D_{ac} = 7.19$ Å and $D_{bc} = 0$ for μ=0 eV at 50 K. Scattering time, τ = 1 ps and Electric field, E = 1 μV/nm applied by an angle θ to the x-axis. **H.** Normalized photoresponse at 0.027, 0.103, 0.278, and 0.443 THz, respectively. **I.** Normalized photoresponse at 0.49, 0.54, 0.74, and 0.82 THz, respectively.

VIII. 2. Terahertz imaging applications for $NbIrTe_4$ Hall rectifier

To further highlight the practical application of our devices, we conduct advanced experiments comparing terahertz transmission imaging with infrared thermal imaging. The ornate metal characters of "China" served as our test objects, which possess dimensions measuring 35mm×70mm and stick on cardboard, depicted in Fig. S18B. Initially, we capture images using a commercial infrared thermal imager, resulting in Fig. S18C, where the metal objects are barely discernible due to their temperature proximity to the ambient surroundings. Subsequently, a gentle palm-warming of the metal objects preceded a re-imaging of the reverse side, yielding a slightly blurred depiction shown in Fig. S18D. In our pursuit to pinpoint distinctive object features, we harness a 0.30 terahertz radiation source, meticulously focusing it onto a Hall rectifier positioned at the focal plane. Throughout this meticulous process, we meticulously document emission power focused on the object, without any bias voltage. Fig. S18E showcases a high-resolution image comprising 100 × 100 pixels (with an integration time of 20 ms per pixel), vividly illustrating the "China" metal lettering with an exceptional signal-to-noise ratio. This demonstrates the significant potential of our device for large-area imaging application.

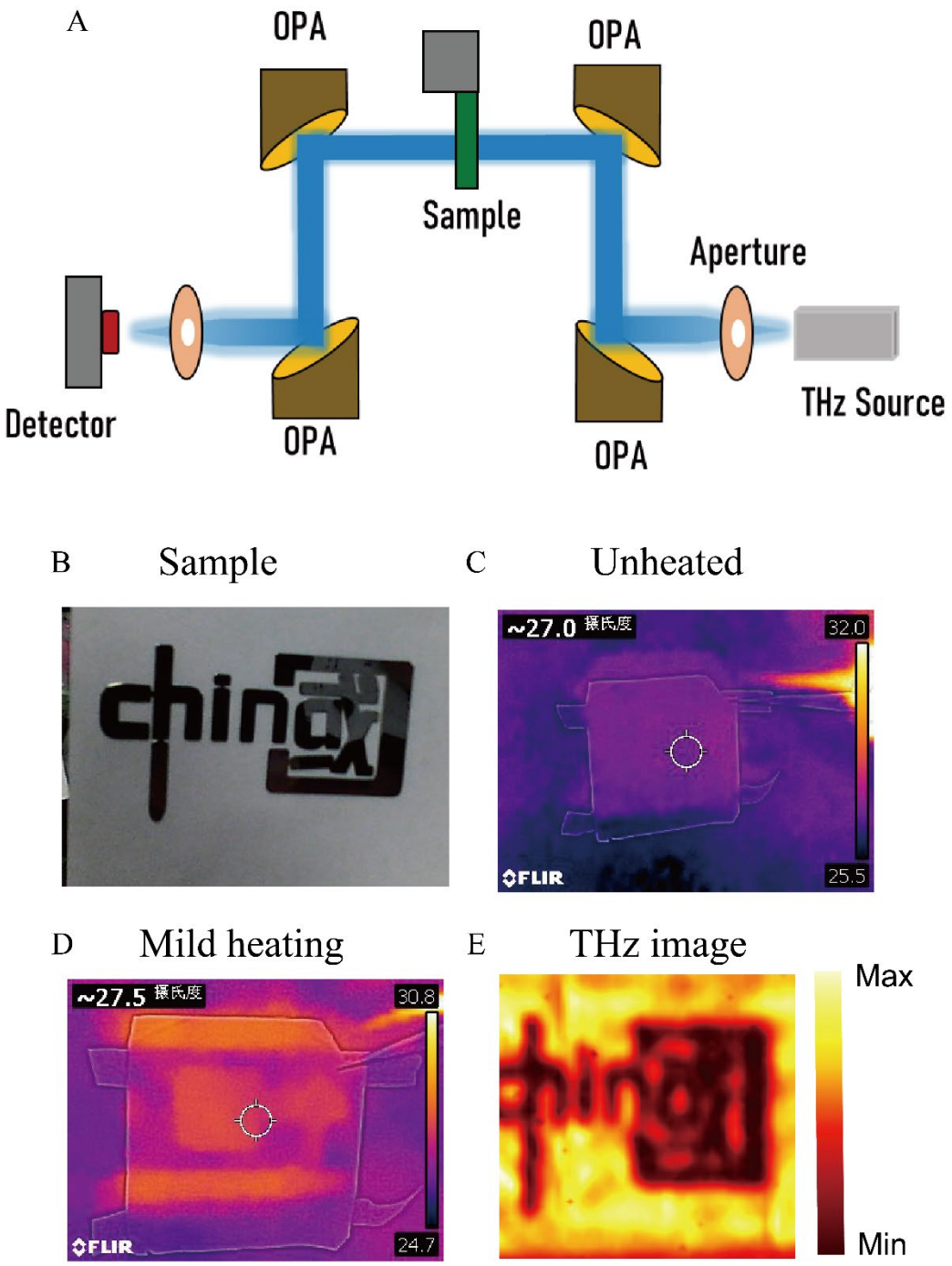

Fig. S18. Terahertz imaging for NbIrTe4 Hall rectifier. **A.** Setup for terahertz imaging experiment. The ornate metal characters of "China" served as our test object. The 0.03THz light source is recorded by converging the beam through the diaphragm and focusing it onto the Hall device through four off-axis parabolic mirrors. **B.** A physical image of object under visible light. **C.** Infrared transmission imaging of an object at ambient temperature. **D.** Infrared transmission imaging of an object gently warmed by a palm at ambient temperature. **E.** Terahertz transmission imaging of objects.

Supplementary references:

1 Shojaei, I. A. *et al.* A Raman probe of phonons and electron-phonon interactions in the Weyl semimetal NbIrTe(4). *Sci Rep* **11**, 8155 (2021).

2 Zhang, J. *et al.* Colossal Room-Temperature Terahertz Topological Response in Type-II Weyl Semimetal NbIrTe(4). *Adv Mater* **34**, e2204621 (2022).

3 Fichera, B. T. *et al.* Second harmonic generation as a probe of broken mirror symmetry. *Physical Review B* **101** (2020).

4 Kumar, D. *et al.* Room-temperature nonlinear Hall effect and wireless radiofrequency rectification in Weyl semimetal TaIrTe(4). *Nat Nanotechnol* **16**, 421-425 (2021).

5 Dames, C. & Chen, G. 1ω,2ω, and 3ω methods for measurements of thermal properties. *Review of Scientific Instruments* **76** (2005).

6 Wang, N. *et al.* Quantum-metric-induced nonlinear transport in a topological antiferromagnet. *Nature* **621**, 487-492 (2023).

7 Du, Z. Z., Wang, C. M., Li, S., Lu, H. Z. & Xie, X. C. Disorder-induced nonlinear Hall effect with time-reversal symmetry. *Nat Commun* **10**, 3047 (2019).

8 Kang, K., Li, T., Sohn, E., Shan, J. & Mak, K. F. Nonlinear anomalous Hall effect in few-layer WTe(2). *Nat Mater* **18**, 324-328 (2019).

9 Gao, A. *et al.* Quantum metric nonlinear Hall effect in a topological antiferromagnetic heterostructure. *Science* **381** (2023).

10 He, P. *et al.* Graphene moiré superlattices with giant quantum nonlinearity of chiral Bloch electrons. *Nature Nanotechnology* **17**, 378-383 (2022).

11 Suarez-Rodriguez, M. *et al.* Odd Nonlinear Conductivity under Spatial Inversion in Chiral Tellurium. *Phys Rev Lett* **132**, 046303 (2024).

12 Hou, D. *et al.* Multivariable scaling for the anomalous Hall effect. *Phys Rev Lett* **114**, 217203 (2015).

13 Luu, T. T. & Worner, H. J. Measurement of the Berry curvature of solids using high-harmonic spectroscopy. *Nat Commun* **9**, 916 (2018).

14 Kaneshima, K. *et al.* Polarization-Resolved Study of High Harmonics from Bulk Semiconductors. *Phys Rev Lett* **120**, 243903 (2018).

15 Lv, Y. Y. *et al.* High-harmonic generation in Weyl semimetal beta-WP(2) crystals. *Nat Commun* **12**, 6437 (2021).

16 Schubert, O. *et al.* Sub-cycle control of terahertz high-harmonic generation by dynamical Bloch oscillations. *Nature Photonics* **8**, 119-123 (2014).

17 Liu, H. *et al.* High-harmonic generation from an atomically thin semiconductor. *Nature Physics* **13**, 262-265 (2016).

18 Ward, J. F. Calculation of Nonlinear Optical Susceptibilities Using Diagrammatic Perturbation Theory. *Reviews of Modern Physics* **37**, 1-18 (1965).

19 Pizzi, G. *et al.* Wannier90 as a community code: new features and applications. *Journal of Physics: Condensed Matter* **32**, 165902 (2020).